DEM analysis on the role of aggregates on concrete strength

P. Wang, N. Gao, K. Ji, L. Stewart, C. Arson*

School of Civil and Environmental Engineering, Georgia Institute of Technology, USA

Abstract

This study aims to understand the micro-mechanisms that drive fracture propagation in concrete and to assess the roles of the strength of aggregates and of the aggregate/mortar interfacial transition zone (ITZ) on concrete strength. We use the Discrete Element Method (DEM) to model concrete samples. Mortar is represented by a volume of bonded spherical elements. Bonds are governed by a new displacement-softening law. Aggregate centroids are randomly placed in the DEM sample. We use CT scan images of real aggregates to plot 3D aggregate contours. The spherical elements that are contained in 3D contours around the randomly placed centroids are replaced by clusters with aggregate properties. The number and the size of the clusters are determined from the experimental Particle Size Distribution. The DEM concrete model is calibrated against uniaxial compression tests and Brazilian tests of both mortar and concrete. It is found that: At same aggregate volume fraction, a concrete sample with randomly placed aggregates and ITZ bonds is stronger; Concrete strength is linearly related to

*Corresponding author.
E-mail address: chloe.arson@ce.gatech.edu
Phone: 404-385-0143

aggregate tensile strength; A linear relationship exists between the contact ratio in the mortar/aggregate ITZ and concrete strength; The ITZ has more influence on concrete strength than aggregate tensile strength.
Keywords:
DEM, concrete strength, aggregates, interfacial transition zone, CT scan, physical tests

---

1. Introduction

The volume of concrete used worldwide is twice that of steel, wood, plastics, and aluminum combined. It is estimated that more than 11 billion metric tons of concrete are used every year [1]. Concrete is composed of coarse aggregates and mortar, which itself is made of fine particles (e.g. sand grains) and cement. With a volume fraction of 40 % to 50 %, coarse aggregates play an important role in concrete mechanical properties [2, 3]. Concrete tensile and compressive strengths are particularly important, because a deficiency in strength can lead to expensive repairs or even structural failure. Zhou and collaborators conducted cube compression tests in concrete with six different types of coarse aggregates, and they found that the compressive strength of the cubic concrete samples can be either higher or lower than that of mortar and that when the aggregates are weak, concrete strength is drastically reduced [4]. Similar results on compressive strength are reported in [3, 5, 6]. Additionally, Beshr and collaborators found that both the compressive and splitting tensile strengths of concrete depend on the type of coarse aggregate (e.g. calcareous, dolomitic, quartzitic limestone, steel slag) [7]. They noted that failure planes in high strength concrete often pass through the

coarse aggregates. A power law was used to characterize the relationship between coarse aggregates' compressive strength and concrete flexural tensile strength. The correlation coefficient, R^2, is in the order of 80 % [8]. However in some other tests, researchers found that concrete tensile strength does not depend on the type of coarse aggregate employed, which might be explained by the fact that the degree of micro cracking (strain softening) around the aggregates is similar for different types of coarse aggregates [2].

Concrete strength is indeed greatly affected by the Interfacial Transition Zone (ITZ) between coarse aggregates and mortar. The ITZ is a region of 15 to 30 μm in thickness, with a low content of cement particles and a high porosity, due to the wall effect [9]. The high local porosity and water content of the ITZ favors the deposition of calcium hydroxide, which, compared with calcium silicate hydrate (C-S-H), is endowed with weaker van der Waals forces and a more oriented micro-structure, which provide less adhesion capacity [1]. As a result, the ITZ is weaker in strength. Zimbelmann conducted a series of tests on ITZ strength and found that the strength is 80 % lower for quartz - Portland cement interfaces than for the cement itself and that the ITZ strength is closely related to the type of coarse aggregate employed [10]. They also proposed that the strength of the ITZ increases with time at the same rate for all types of coarse aggregate. Three-point bending and compression tests were conducted on concrete that contained coarse aggregates coated with paraffin, for which the adhesion at the interface was eliminated [11]. Results showed that tensile strength, compressive strength as well as the stress intensity factor all dropped by approximately 40 to 60 %. The shape and surface texture also play an important role in the bonding

strength [12, 13].

Continuum mechanics models based on the theory of elasticity and plasticity cannot explicitly predict the occurrence of micro-cracks in concrete. Several numerical techniques exist to alleviate this limitation and account for the spatial randomness brought by the coarse aggregates [14, 15]. Wriggers and Moftah modeled concrete with the Finite Element Method (FEM). They generated a distribution of spherical coarse aggregates with the Monte Carlo's simulation method and implemented an isotropic damage model in the FEM to predict fracture propagation [16]. They found that damage first occurs around the aggregates and then propagates within the mortar. X. Wang and collaborators used cohesive zone elements to model fracture initiation and propagation and to study the effect of meso-structure on damage and failure in concrete [17]. Results show that concrete strength decreases with increasing aggregate content and that neither the concrete strength or the pre-peak response is sensitive to the aggregate distribution. Cohesive zone elements were also employed to analyze fracture propagation in concrete [18, 19, 20]. Recently, the Discrete Element Method (DEM) was used to model concrete at the mesoscale because of its simplicity regarding crack representation [21, 22]. Mortar and aggregate constituents were modeled by bonded spherical particles with different mechanical properties and cracks are represented by bond failures. One advantage of the DEM is that the morphology of the coarse aggregates can be easily represented from the images of real aggregates [23, 24]. In this study, we use the DEM to analyze the influence of coarse aggregates on concrete strength.

A common issue encountered with DEM bonded particle models is that

the predicted strength ratio uniaxial compressive strength / Brazilian test strength (UCS/BTS) is much lower than the strength ratio determined experimentally [25]. Potyondy and Cundall obtained a UCS/BTS ratio of 4.5 (respectively 7.2) with PFC2D (respectively PFC3D), compared to 21.5 for granite [26]. Similar shortcomings are reported in [27] and [28]. To overcome this problem, it was proposed to use angular clumps or clusters that increase particle interlocking [26, 29], but the introduction of complex-shaped particles brings heterogeneity, anisotropy and scale effects [25]. Attempts were made to increase the UCS/BTS ratio with a variety of contact models. For instance, by partially [25] or completely [30] ignoring the contribution of bending moments and twisting moments in the parallel bond model [31], the strength ratio can be greatly improved. However, this modeling approach lacks physical meaning. Inspired by the cohesive crack concept, softening models were developed at particle scale to simulate fracture propagation in rocks and concrete while ensuring a high strength ratio [32, 33, 34]. Kim and collaborators proposed a 2D bilinear cohesive softening model which can successfully capture crack initiation and size effects in asphalt concrete [35]. Recently, Ma and Huang proposed a displacement-softening model that allows simulating fracture proapgation with a strength ratio of up to 30 while capturing the failure mechanism in different tests [36]. However, in all the softening models proposed to date, the introduction of empirical parameters, in particular the softening displacement or the softening coefficient, lacks physical meaning and makes calibration challenging. In this paper, we propose a new displacement softening contact bond model to overcome these limitations.

Cracks in concrete occur at different scales, due to structural loading, thermal gradients, shrinkage or wet/dry cycles. Large tensile cracks (width>0.1 mm) can be controlled by proper design, e.g. by embedding steel reinforcements in concrete structural members. But micro-cracks, which usually exist at the aggregate-cement interface, are much harder to control. The objective of this study is, therefore, to understand the micro-mechanisms that drive fracture propagation in concrete and assess the influence of aggregates on concrete strength. We take the example of the concrete used by the Georgia Department of Transportation for infrastructure construction. We first present a series of uniaxial compression and Brazilian splitting tests conducted on mortar and concrete samples. We then describe the construction of our DEM concrete model. After explaining the calibration of the DEM model, we analyze the sensitivity of concrete strength to the shape and strength of the coarse aggregates and to the strength of the aggregate/mortar ITZ.

2. Experimental study of concrete and mortar strengths

2.1. Materials

The concrete used in the experimental study followed the Georgia Department of Transportation specifications for pre-stressed concrete (GDOT, 2013) and consisted of Type I cement, water, fine aggregates, and coarse aggregates. We used size 67 granite-gneiss coarse aggregates from Norcross, Georgia (distributed by Vulcan Materials Company). The granite-gneiss aggregates are formed as a banded combination of an igneous rock (granite) and its metamorphic rock counterpart in gneiss. Both rocks are primarily composed of strained and microcrystalline quartz. The concrete had the

mixture weight fractions and properties listed in Table 1. The concrete was delivered to the site via a ready mix truck. Upon delivery, a slump test was conducted and yielded a result of 8.25 cm.

Table 1: Concrete mix used in the experiments.

Materials	Weight fraction (%)	Details
Cement	18.6	Type I
Water	5.3	
Fine Aggregate	28.3	Specific Gravity = 2.69
Coarse Aggregate	47.8	Specific Gravity = 2.71

The mix design of the mortar was very similar to the mix design used in the concrete experiments. The mortar samples were made using the same ratio of water to cement (0.38). The mortar mix design is given in Table 2.

Table 2: Mortar mix used in the experiments.

Materials	Weight fraction (%)	Details
Cement	36.0	Type I
Water	14.0	
Fine Aggregate	50.0	Specific Gravity = 2.69

2.2. Methods

The Brazilian test (BT) is an ASTM standard test method used to determine the splitting tensile strength of cylindrical concrete specimens [37].

A disc-shaped specimen is compressed between two diametrically opposite loading strips. Tensile stress develops at the center of the specimen [38]. Because the procedures are simple and the specimen preparation is easy, the Brazilian test has been widely used as an indirect method to test the tensile strength of concrete and rock. The tensile strength, σ_t, is given by:

$$\sigma_t = \frac{P}{\pi R t} \tag{1}$$

where P is the peak load and R and t are the radius and the thickness of the specimen, respectively.

The uniaxial compression test (UCT) is used to measure the compression strength of cylindrical mortar/concrete specimens under zero confining stress. The uniaxial compressive strength (UCS), σ_c, is given by:

$$\sigma_c = \frac{P}{\pi R^2} = \frac{P}{A_0} \tag{2}$$

where A_0 is the initial cross sectional area of the specimen.

Mortar and concrete samples used for the BTs were 150 mm in diameter and 100 mm in thickness (150 $\times$ 100). The ratio of diameter/thickness was chosen so as to avoid size effects [39, 40]. Mortar samples used for the UCTs were 100 mm in diameter and 200 mm in thickness (100 $\times$ 200). All cylinders were cast and stored in a fog room for 28 days before the tests. Concrete specimens used for the UCTs were 150 mm in diameter and 300 mm in thickness (150 $\times$ 300). Concrete tests were performed after a period of 28 days of curing time.

2.3. Brazilian tests and uniaxial compression tests done on mortar

Three Brazilian tests and three uniaxial compression tests were conducted. Results are shown in Figures 1 and 2, in which horizontal red dash

lines represent the average values of the peak stresses. A brittle failure was observed both in the BTs and the UCTs: stress increases with the strain until a peak value (strength) is reached, after which stress drops abruptly. The average Brazilian tensile strength was 4.71 MPa and the average compressive strength was 61.42 MPa. Less than 10% variability was noted for both BT and UCT strength results.

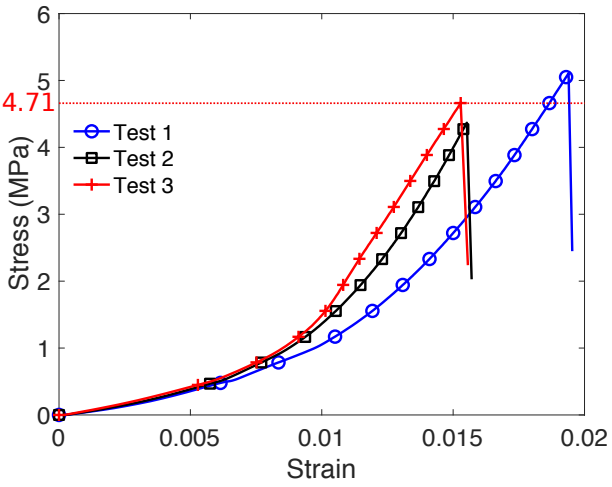

Figure 1: Stress-strain curves of mortar cylinders in the Brazilian tests

Figure 3 shows typical pictures of a mortar sample that fails during a BT. We can see shear cracks close to the loading platens and a tensile crack developing at the center of the specimen, as shown in Figure 3(a). As the compressive force increases, the tensile crack propagates towards the loading points and the sample breaks into two main parts, as shown in Figure 3(b). This tensile failure mode was observed in previous research [41]. In the UCTs, we observed mixed mode failure caused by the combination of shear and vertical fractures (Figure 4(a)), as well as shear failure (Figure 4(b)).

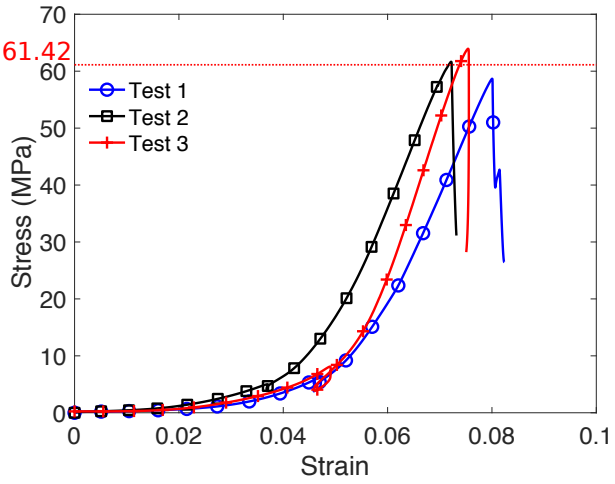

Figure 2: Stress-strain curves of mortar cylinders in the uniaxial compression tests

Both of these types of failures are very common in UCTs [42, 43]. There is a significant variability of failure modes in UCTs, mainly due the variability in microstructure and microcrack distributions among specimens [44], although failure variability was also noted among identical samples [45]. Despite the acknowledged failure variability expected in the UCTs, the UCTs that we conducted on mortar yielded a similar strength value – which we used later for the calibration of our DEM model.

2.4. Brazilian tests and uniaxial compression tests done on concrete

We performed three BTs and three UCTs on concrete. Test results are shown in Figures 5 and 6. Concrete specimens exhibited a quasi-brittle behavior. The average Brazilian tensile strength was 2.46 MPa and the average compressive strength was 32.53 MPa, which correspond, respectively, to 57% of the tensile splitting strength of mortar and to 53% of mortar compressive strength. In the BTs, concrete cylinders failed in tension, in a similar way

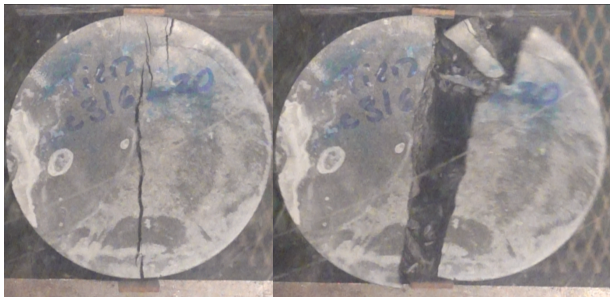

Figure 3: Typical failure observed for mortar cylinders subjected to Brazilian Tests.

Figure 4: Typical failure modes observed during the uniaxial compression tests on mortar cylinders ((a) and (b)) and on concrete cylinders ((c) and (d))

as the mortar samples (see Figure 3). In the UCTs, we observed either shear failure (Figure 4(c)) or columnar vertical failure (Figure 4(d)). By observing the fracture surfaces after the tests, we found that fractures had propagated in mortar, in the aggregates and at the mortar/aggregate interfaces. A large number of aggregates were crushed and new fracture surfaces had appeared in the aggregates (Figure 7). These observations differ from previous experimental results reported in the literature [46], in which it was noted that fractures are more likely to propagate at the ITZ. We hypothesize that these differences are due to differences in aggregate properties. This assumption is tested in the simulations presented in the following. Table 3 summarizes the average strength results.

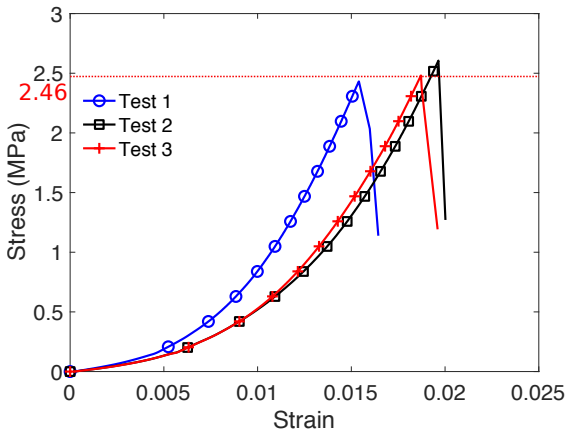

Figure 5: Stress-strain curves of concrete cylinders in the Brazilian tests

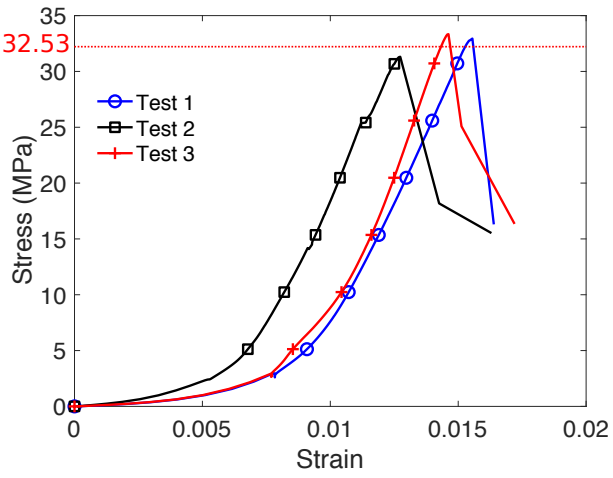

Figure 6: Stress-strain curves of concrete cylinders in the uniaxial compression tests

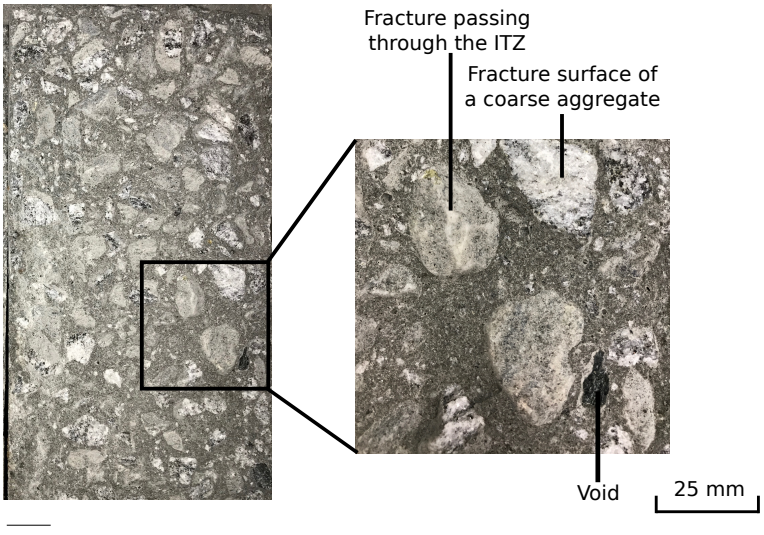

Figure 7: Open surface of a concrete specimen after a Brazilian test, showing fractures passing through both coarse aggregates and ITZ.

Table 3: Average tensile splitting strength and uniaxial compressive strength for the mortar and concrete specimens

Materials	Tensile strength (MPa)	Uniaxial compressive strength (MPa)
Mortar	4.71	61.42
Concrete	2.46	32.53

3. Discrete element model construction

In order to capture the behavior of mortar with the Discrete Element Method (DEM), we propose a new bond displacement-softening law that we implement in the DEM code PFC3D developed by Itasca [31]. We then describe a method to model concrete with the DEM. Coarse aggregates are represented by particle clusters of realistic shape, and mortar is represented by bonded spherical particles. First, we generate a sample made of bonded spherical rigid elements, in which the bonds are modeled with the new displacement-softening law. Aggregate centroids are then randomly placed in the DEM sample. We use CT scan images of real aggregates to plot 3D aggregate contours. The spherical elements that are contained in 3D contours around the randomly placed centroids are replaced by clusters. The number and size of the clusters are determined from the experimental Particle Size Distribution (PSD) of the aggregates.

3.1. A new displacement softening contact bond model

The mechanical properties of the spherical elements that make a DEM model are the normal stiffness k_n, the normal/shear stiffness ratio k_n/k_s, the

friction coefficient μ and the mass density ρ. Bonds between the spherical elements are breakable, which allows capturing crack propagation in the DEM sample. Experimental results reported in numerous studies indicate that, after the maximum load has been reached, concrete exhibits a gradual decrease of loading capacity with increasing strain/displacement [47, 48, 49]. To capture this softening behavior, we propose a displacement-softening contact model, inspired by the bond model proposed by Ma and Huang [36]. Figure 8 illustrates the normal and shear force-displacement curves employed in the proposed new contact model, which is governed by the following five microparameters: normal loading stiffness k_{nl}, maximum normal force F^n_{max}, normal softening stiffness k_{ns}, bond stiffness ratio k_{nl}/k_{sl} and maximum force ratio F^s_{max}/F^n_{max}. The maximum normal force F^n_{max} is given by:

$$F^n_{max} = \pi(R_1 + R_2)^2\sigma_t/4 = A_0\sigma_t, \tag{3}$$

where R_1 and R_2 are the radii of the two particle in contact; σ_t is the bond tensile strength; A_0 is the bonding area. Equation 3 is based on the assumptions that the bonding area between two spherical particles has a disc shape with a radius equal to the average radius of the two particles in contact. The maximum tensile force that a bond can carry is the product of the bonding area by the tensile strength. The maximum force ratio F^s_{max}/F^n_{max} is equal to the bond strength ratio τ/σ_t. Therefore, two sets of micro-properties are used in our DEM simulations, i.e. the micro-properties of the particles:

$$\{k_n, k_n/k_s, \mu, \rho\} \tag{4}$$

and the micro-properties of the displacement softening contact bond model:

$$\{k_{nl}, \sigma_t, k_{ns}, k_{nl}/k_{sl}, \tau/\sigma_t\}\,. \tag{5}$$

The relationships between the above micro-properties and the macroscopic properties of the mortar and concrete DEM samples are discussed below.

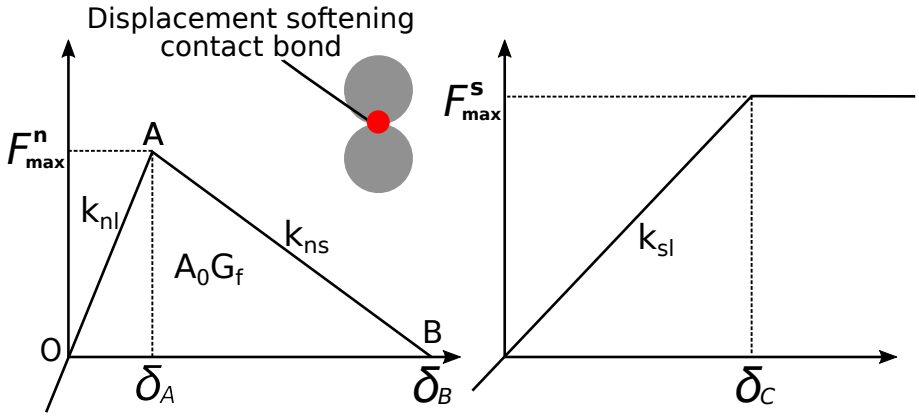

Figure 8: Force-displacement relationships used in the displacement softening contact bond model. k_{nl} is the normal loading stiffness; F^n_{max} is the maximum normal force; k_{ns} is the normal softening stiffness; k_{nl}/k_{sl} is the bond stiffness ratio; F^s_{max}/F^n_{max} is the maximum force ratio.

In our analysis, we followed the method proposed in [26] and [50] to define particle microparameters, as follows:

$$k_n = 4RE, \tag{6}$$

$$k_n/k_s = E/G, \tag{7}$$

$$\rho = (1+n)\rho_{mat}, \tag{8}$$

where R is the particle radius; E and G are the Young's modulus and shear modulus of the material represented by the DEM sample, respectively; ρ_{mat} is the mass density of the material and n is the porosity of the DEM specimen (around 35% in 3D simulations).

The normal loading stiffness k_{nl} is set equal to the average of the normal stiffnesses of the two bonded spherical elements. The bond tensile strength is set equal to the tensile strength of the material represented by the DEM sample. In our displacement softening contact model, the bond shear strength is set much higher than the tensile strength so that shear stress does not affect the bond breakage. This is a realistic hypothesis for DEM models of bonded and aggregated materials, according to [51, 34]. The energy required to break a bond is equal to the product of the fracture energy, G_f, by the bonding area, A_0. Therefore, based on the geometry of the left part of Figure 8, the normal softening stiffness k_{ns} is expressed as:

$$k_{ns} = \frac{(F^n_{max})^2 k_{nl}}{2G_f A_0 k_{nl} - (F^n_{max})^2}. \tag{9}$$

The remaining two contact bond parameters, k_{nl}/k_{sl} and τ/σ_t, control the shear behavior of the material. In former studies [51, 34, 25], a realistic ratio between the uniaxial compressive strength and the Brazilian tensile strength (between 10 to 20 for most geomaterials) could be obtained with a high stiffness ratio. Here, we calibrate k_{nl}/k_{sl} and τ/σ_t against experimental results. To summarize, the required micro-properties in Equation 4 and 5 can be expressed in the form:

$$\{E, G, \mu, \rho_{mat}, \sigma_t, G_f, k_{nl}/k_{sl}, \tau/\sigma_t\} \tag{10}$$

3.2. Generation of the mortar sample

We generated the cylinder specimens with the method proposed in [26], which will be briefly introduced here. In a first step, an assembly of particles is generated in a material vessel. The number of particles generated depends

on the volume of the vessel, an estimated porosity (35% in this 3D model) and the given average particle size. Initially, all particles are randomly located and may overlap. Then the radii of all particles are modified uniformly so that an isotropic target stress, which is set to 1% of the uniaxial compressive strength, can be achieved at all boundaries. Large overlaps between particles are eliminated and force chains are generated. Particles with a coordination number (i.e., a number of contacts with neighboring particles) less than 3 are defined as "floating" particles in the sample. A densely packed sample can be generated by increasing the radii of these particles. Once the DEM sample is generated with the required porosity, the new displacement softening contact bond model presented in Subsection 3.1 is assigned to all particle-to-particle contacts. Lastly, we remove the bounding walls and relax the material.

In our simulation, a cuboid mortar sample is first generated and then cut into the desired size and shape – in this case, 150 × 100 cylinders for BTs and 100 × 200 cylinders for UCTs, like in the experiments. The minimum particle size was 1 mm and the size ratio between the maximum particle size and the minimum particle size was 1.66. In each simulation, we had 120,000 to 130,000 particles and it usually took 12 hours on a workstation (i7-3770 3.4GHz CPU and 64 GB RAM) to simulate one test.

3.3. Generation of the concrete sample

In order to generate realistic aggregate shapes, we scanned 20 representative aggregates with an X-ray scanner. Aggregate shapes were characterized by 20,000 to 30,000 points, which provided detailed information about particle shapes and surface textures. Figure 9 shows the original scan data and the corresponding DEM shapes obtained for four aggregates.

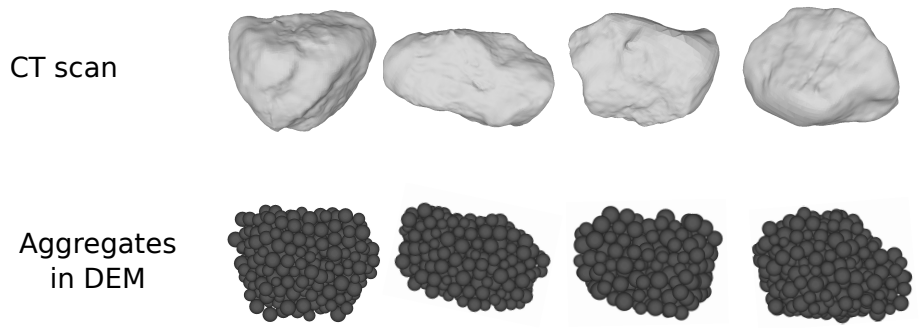

Figure 9: Generation of aggregate shapes in the DEM model

The DEM concrete model is generated as follows:

1. Create the mortar sample using the method presented in Section 3.2.
2. Calculate the number, sizes and positions of the aggregates. The number of coarse aggregates in each fraction size, n_i is given by

$$n_i = V_t \eta (P_{2i} - P_{1i})/V_i \tag{11}$$

where V_t is the total volume of the specimen; η is the volume fraction of the coarse aggregates; P_{1i} and P_{2i} are the percentage of aggregates finer than d_{1i} and d_{2i} in the PSD curve, respectively; V_i is the average volume of an aggregate in this size fraction. Within each size fraction, the size of an aggregate is assumed to follow a uniform distribution. A MATLAB code was written to generate non-overlapping spheres within the sample boundary, with the given number of aggregates and the given aggregate sizes. Each sphere generated by the MATLAB code corresponds to an aggregate of specific volume.

3. Replace the spheres by realistic aggregate shapes. We replace each sphere with a realistic shape randomly chosen from the set of shapes ob-

tained by X-ray scanning (here, we used 20 different aggregate shapes). After the substitution, some aggregates may overlap, which slightly decreases the total volume fraction of the aggregates. In addition, some aggregate fractions may be outside of the boundary of the specimen.

4. Identify the spherical elements and the contacts that belong to the aggregates. Another MATLAB algorithm is created to loop through all spherical elements and contacts, and check whether they belong to an aggregate or not. Then the aggregate volume fraction is calculated as the ratio of the number of spheres in the aggregates by the total number of spheres in the specimen. We compare this volume fraction with the volume fraction found experimentally, update the parameter η accordingly, and repeat steps 2 to 4 if the difference is larger than 1%.
5. Change the properties of the spherical elements and bonds within the aggregate contours and in the ITZ. Two strategies are compared to model the ITZ: bond deletion and bond weakening (see Subsection 4.2).
6. Generate voids. Another important difference between mortar and concrete is the void ratio. An estimated void ratio of 4% is used in our concrete model, which is a reasonable estimation according to images of X-ray Computed Tomographic images obtained in [52].

Figure 10(a) and (b) show the DEM concrete samples used to simulate the BTs and UCTs, respectively.

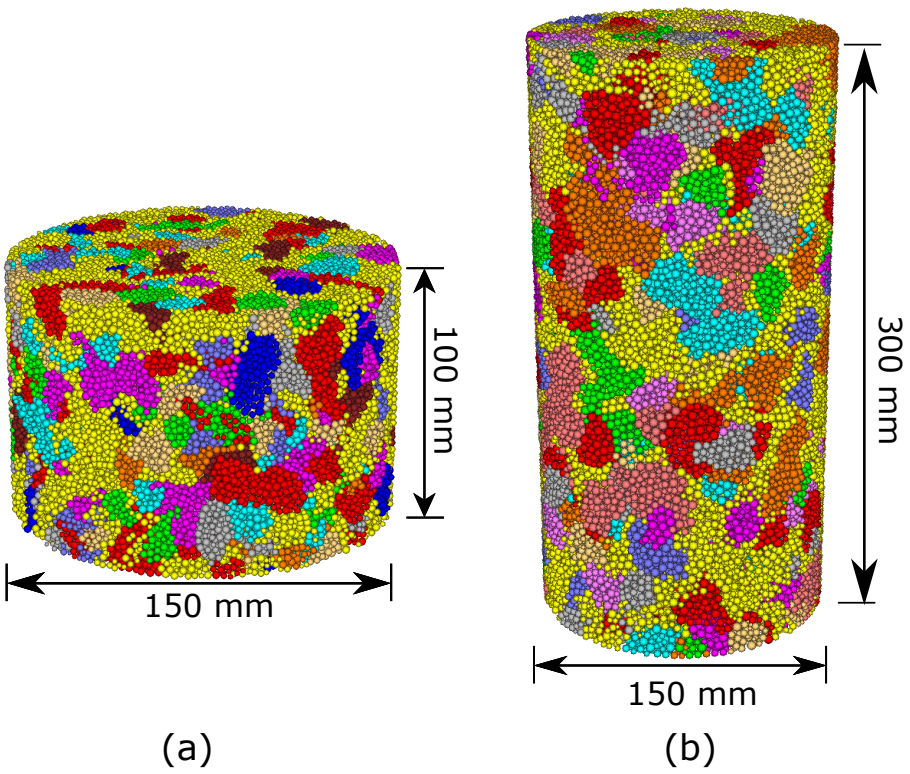

Figure 10: DEM concrete specimens used to simulate (a) Brazilian tests and (b) Uniaxial compression tests

4. Calibration of the DEM concrete model

4.1. Mortar model calibration against experimental results

We obtain the mortar's Young's modulus from the empirical equation proposed in ACI 318 [53]:

$$E = 4700\sqrt{f'_c}, \tag{12}$$

where f'_c is the uniaxial compressive strength, reported in Table 3. Following [1], we assume that the mortar's Poisson's ratio is 0.2. The shear modulus G is then given by $E/(2(1+\mu))$. For the DEM friction coefficient, we use an empirical value of 0.5, as recommended in the state of the art [54]. The mass density of the particles used in the mortar DEM model is calculated from Equation 8. The tensile strength of the bonds, σ_t, is set equal to that of the mortar specimen. Due to the size effects that occur in Brazilian tests, the tensile strength reported in Table 3 is higher than the tensile strength of the material tested [55]. We use the relationship proposed in [56] to calculate mortar tensile strength from the BT strength and from the specimen diameter. For mortar, the fracture energy, G_f, ranges from 20 N/mm to 200 N/mm, depending on the type of mortar [39, 57, 58, 59, 60]. In our simulation, we use $G_f = 80$ N/mm, because this value provides the best fit with experimental results. With the DEM, it is challenging to simulate BTs and UCTs with a realistic ratio uniaxial compressive strength over Brazilian strength (UCS/BTS). Different methods were used in previous studies, for example by generating angular particles to increase the interlocking forces, by increasing the initial compressive strength, by modifying the strength ratio, or by creating new contact models [34, 51, 25]. In our displacement softening contact model, the ratio of UCS/BTS is mainly controlled by two

parameters: k_{nl}/k_{sl} and τ/σ_t. Mortar parameters obtained after calibration are summarized in Table 4.

In a Brazilian test, the failure mechanism is a combination of shear failure close to the loading platens and tensile failure at the center [41]. A low k_{sl} decreases the shear stress at failure, thus yielding a lower Brazilian tensile strength. A large τ/σ_t increases the shear strength measured in the uniaxial compression test, but does not exclude the possibility of shear failure at the sample scale, which can also come from the coalescence of tensile micro-cracks [61]. For example, a prior DEM study showed that during a compression test, shear failure occurred while the number of tensile micro-cracks was fifty times higher than that of the shear micro-cracks [62].

Table 4: Mortar and concrete DEM model parameters

Parameter	Mortar	Aggregate
Young's modulus E (GPa):	36.8	36.8
Shear modulus G (GPa):	30.7	30.7
Friction coefficient μ (-):	0.5	0.5
Density ρ_{mat} (kg/m^3):	2400	2400
Tensile strength σ_t (MPa):	3.85	3.5
Fracture energy G_f (N/m):	80	72.7
Stiffness ratio k_{nl}/k_{sl} (-):	6.0	6.0
Strength ratio τ/σ_t (-):	20	20

We conducted the simulations of the UCT and the BT twice to check that DEM randomization effects would not affect the calibration results.

Simulation results are presented in Figures 11 to 14. The BTS and UCS are in agreement with the strengths measured experimentally, with an error of less than 5 %. The ratio of UCS/BTS, which is around 13.0 in our experiments, is properly reproduced in the DEM simulations. Figure 12 shows the location of broken bonds at several stages of the BTs. At 50% of the peak load, micro-cracks appear near the loading platens, which is typical of a local shear mechanism close to the loading supports. At 90% of the peak load, the number of cracks near the loading platens increase. In addition, micro-cracks appear at the center, which reveals a tensile failure mechanism, induced by horizontal tensile stress. At the peak load, the micro-cracks which originated at the center propagate towards the loading platens. After the peak, the specimen rapidly breaks into two fragments. The failure mechanism observed in the simulation, in which the sample fails due to the tensile crack initiated at the center, is thus the same as the failure mechanism observed in the experiments (Figure 3).

In the UCT, we observe randomly distributed micro-cracks at 50% of the peak load. No obvious shear band or fracture can be identified at this point. When the load reaches 90% of the peak load, we can observe more micro-cracks, preferentially oriented along the directions of two shear failure planes (shear bands). At this loading stage, the stiffness of the material starts to decrease due to material softening induced by micro-crack propagation. As we continue loading from 90% to 100% of the peak load, the number of broken bonds in the shear bands increases rapidly. Figure 14 clearly shows a fracture pattern characterized by more than one oblique plane. This failure mode, which is often called double shear, is one of the four most common failure

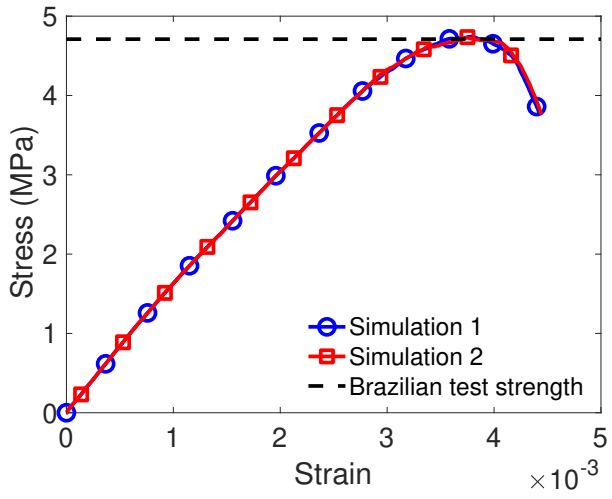

Figure 11: Stress-strain curves of mortar in the Brazilian tests simulated by the DEM

modes reported by ASTM codes [43], along with diagonal fractures, columnar vertical cracks and the combination of conic and vertical cracks. In the experiments (Figure 4), mixed mode failure and shear failure were observed. Failure mode in uniaxial compression is influenced by end constrains [42, 63] as well as sample microstructure [44, 64]. The difference in failure mode between the experiments and the numerical simulation may indeed come from the boundary conditions: in the experiment, the rough surface of the sample is in contact with the rubber loading platen; in the simulation, a fixed lateral displacement was imposed at the interface between the sample an the loading platen, which is a stiffer end constraint. According previous research, the observed double shear failure mechanism is typical of fixed ends boundary conditions [65, 66].

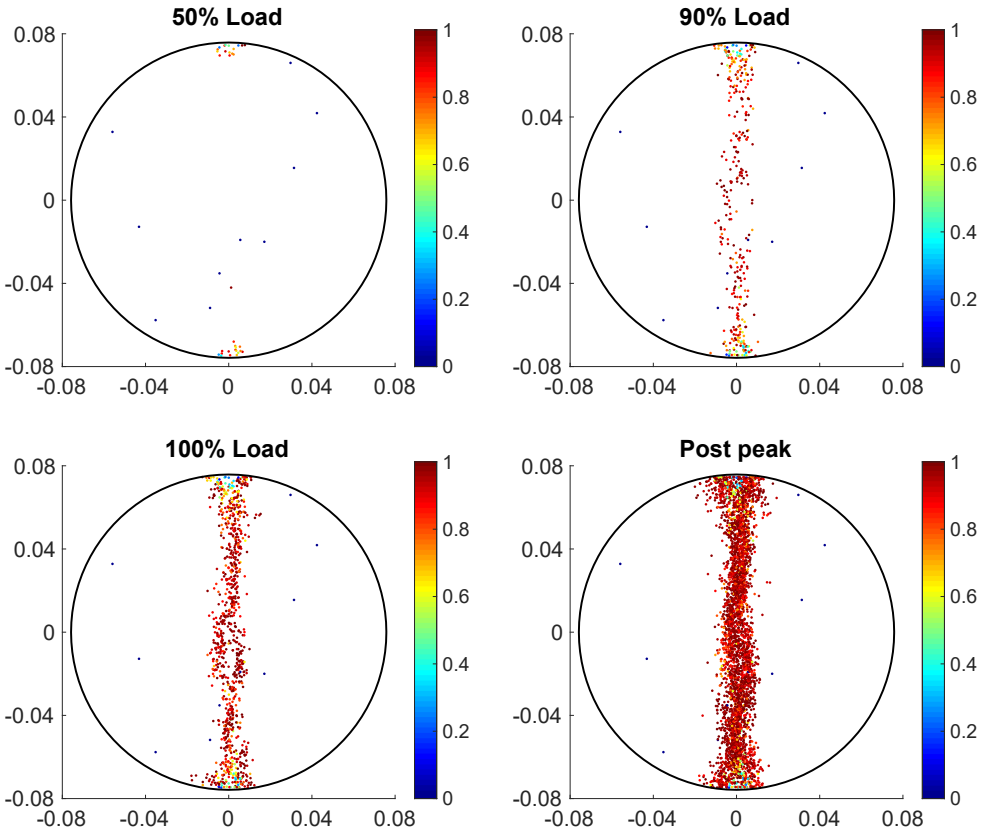

Figure 12: Micro-cracks in mortar at different stages of the Brazilian tests

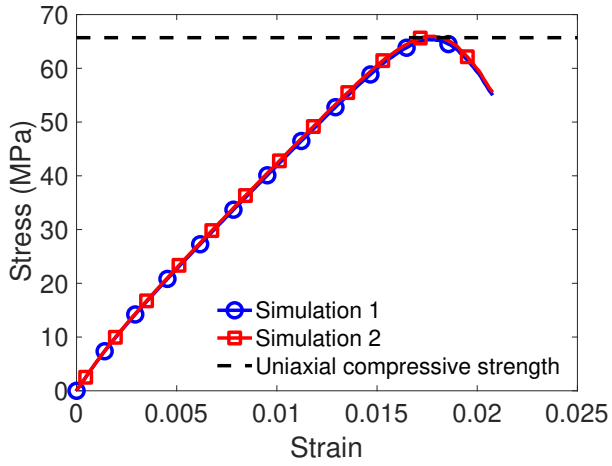

Figure 13: Stress-strain curves of mortar in the uniaxial compression tests simulated by the DEM

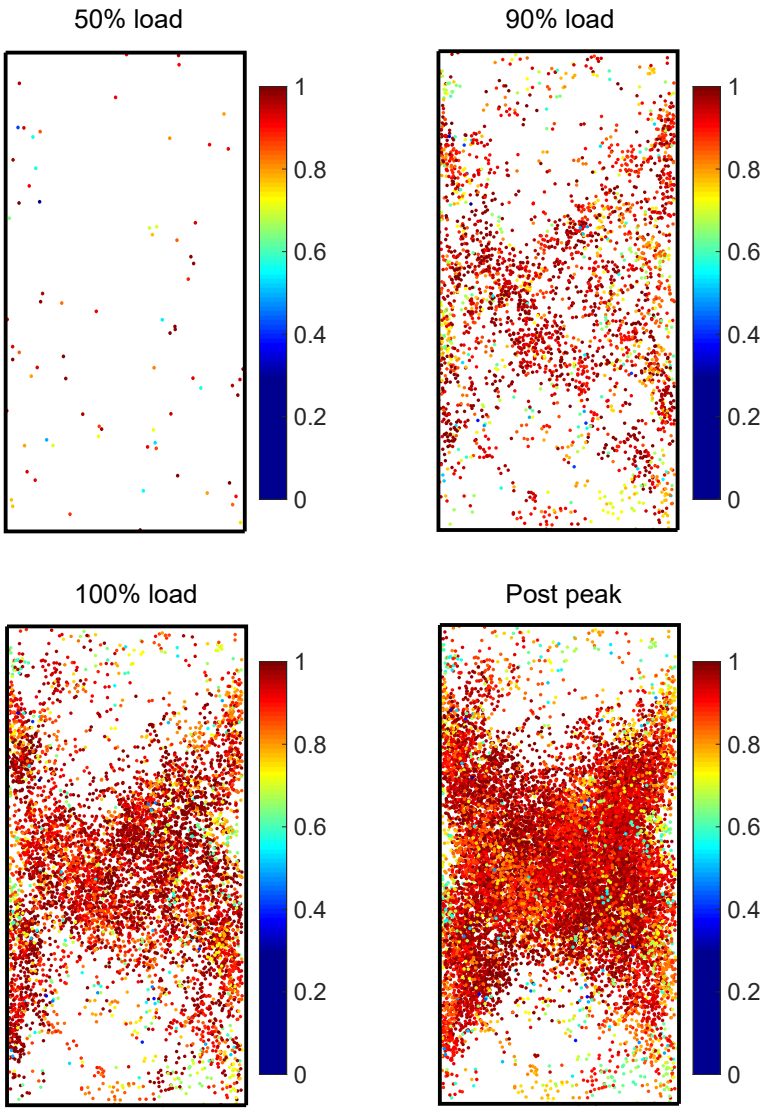

Figure 14: Micro-cracks in mortar at different stages of the uniaxial compression tests

4.2. Concrete model calibration against experimental results

DEM concrete samples were generated according to the method explained in Subsection 3.3. Within the domains identified as aggregates, particles were assigned the same properties (including modulus) as in the mortar domain. The aggregate bonds were assigned the softening contact model, initially with the same bond properties as those of mortar. The ITZ was modeled as a weak interface between the mortar and aggregate particles, either by uniformly weakening the aggregate bonds or by deleting some of the bonds. The aggregate bond properties were then calibrated iteratively to match the concrete splitting and compression strengths obtained numerically with the strengths measured experimentally.

In most concretes, coarse aggregates are found to be much stronger than mortar and have a much lower probability to break [46, 67]. Contrary to those observations, in both the BTs and UCTs that we conducted, a large number of coarse aggregates were crushed and fresh aggregate surfaces were exposed, which indicates that aggregates had a lower tensile strength and a lower compressive strength than mortar. The existence of coarse aggregates leads to a local increase in porosity and thus to a smaller bond area between aggregates and mortar. To account for the effect of the ITZ, we removed 20% of the displacement softening contact bonds between aggregate particles and mortar particles (removal bond method). This value of 20% was obtained by trial and error (the effect of this ratio on concrete strength is discussed in the next section). Not surprisingly, our calibration simulations yielded a lower bond strength σ_t for coarse aggregates than for mortar. In addition, we assume that the ultimate bond displacement at failure is the same as that

of mortar, so that the fracture energy of the aggregates, G_f, is proportional to the aggregate bond strength. The coarse aggregate properties obtained after calibration with the removal bond method are summarized in Table 4.

After calibrating the concrete model with the removal bond method, we repeated the BT and UCT simulations with a different ITZ model, in which the strength of the bonds of the mortar/aggregate interface is uniformly lowered by 20% (weak bond method), all other model parameters set equal. Figures 15 and 16 show that, with all mechanical and geometric parameters set equal, the DEM model with uniformly weaker bonds predicts higher concrete strength than the DEM model of porous ITZ with deleted bonds. This is because a weaker, softening bond can still carry some load after the bond stress exceeds the bond strength. As a result, a higher stress or force is needed to break the concrete sample according to the model with weaker bonds. Considering the fact that the porous structure of the ITZ in real concrete cannot carry any load, we decide to use the removal bond method in our model, and we use the calibrated model parameters presented in Table 4.

We conducted the BT and UCT simulations three times, to check if DEM randomization would have any effects on the results. Simulation results are shown in Figures 15 to 18. Concrete stress-strain curves are similar to those of mortar. However, because the coarse aggregates increase the heterogeneity of the specimens, a variability of 16.0% (respectively 7.0%) is observed for the BTS (respectively UCS) among the three simulations (Figures 15 and 16). In the BT, the sequence of bond breakage events as well as the failure mode in concrete are similar to those in mortar. In the BT, micro-cracks first

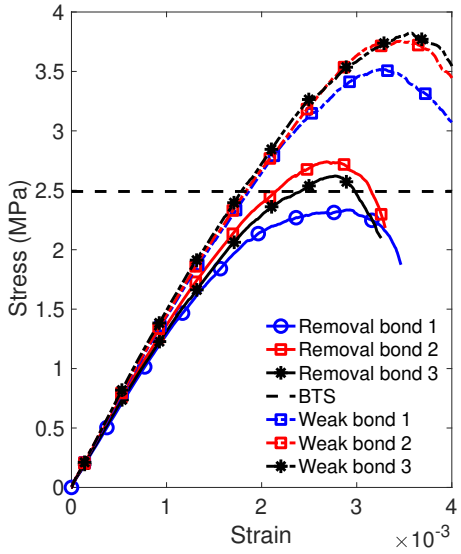

Figure 15: Stress-strain curves of concrete in the Brazilian tests simulated with the DEM

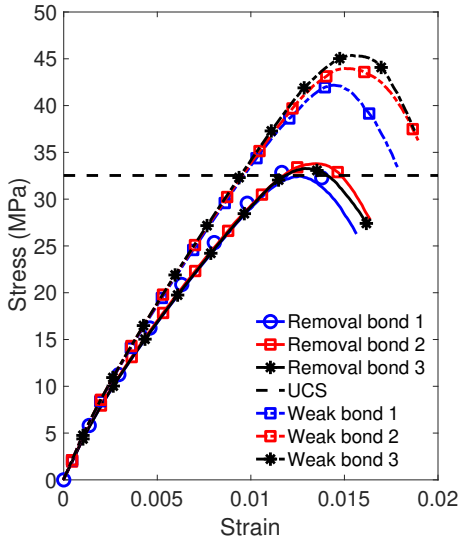

Figure 16: Stress-strain curves of concrete in the uniaxial compression tests simulated with the DEM

appear at the loading platens but the failure is caused by tensile micro-cracks that originate at the center of the specimen and then propagate towards the platens. The failure plane after the peak load is not a straight line, because of the specimen heterogeneity induced by the presence of aggregates. In the UCT, a double shear failure is observed, see Figure 18. Due to the lower loading capacity of concrete, the number of micro-cracks is less than that in mortar. In other words, fractures form at an earlier stage, passing through the weak aggregates and the ITZ. A detailed analysis of the influence of the relative fraction of inactive bonds at the ITZ is presented in the next section.

Note that our modeling approach is limited by the lack of experimental measures on the aggregates employed in the concrete tested. DEM concrete specimens are essentially DEM mortar specimens in which bonds are made weaker within a zone that represents the actual geometry of the aggregates, and in which the mortar/aggregate interface is represented by a fraction of broken bonds.

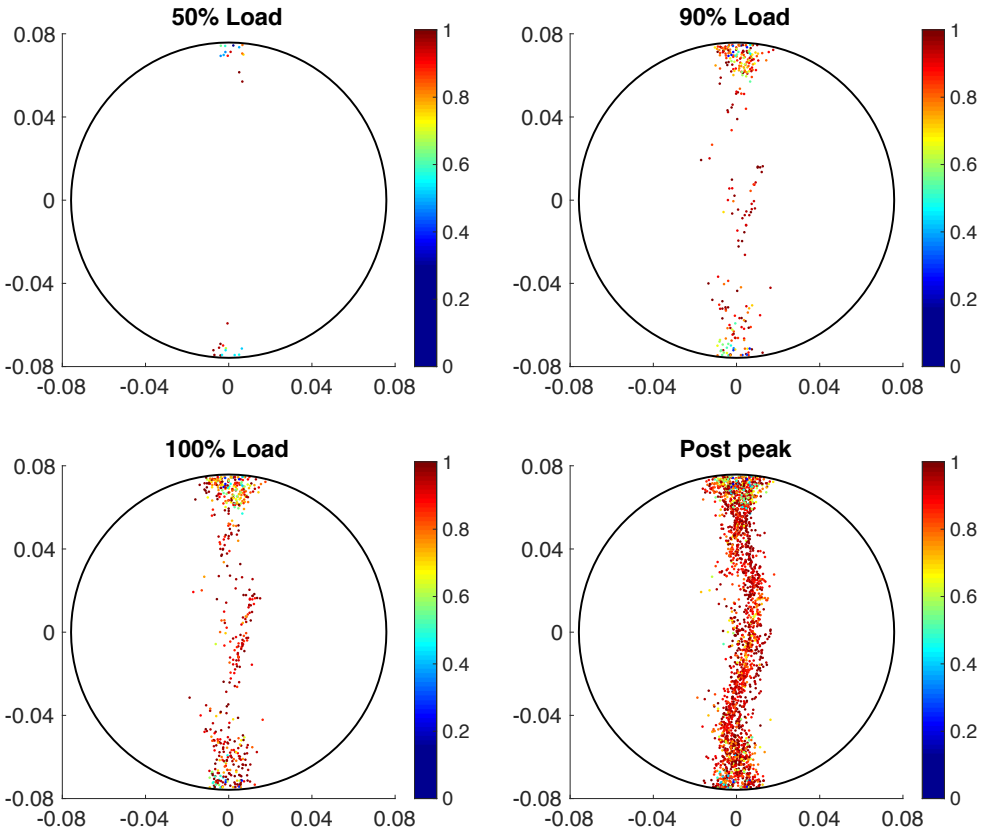

Figure 17: Micro-cracks in concrete at different stages of the Brazilian tests

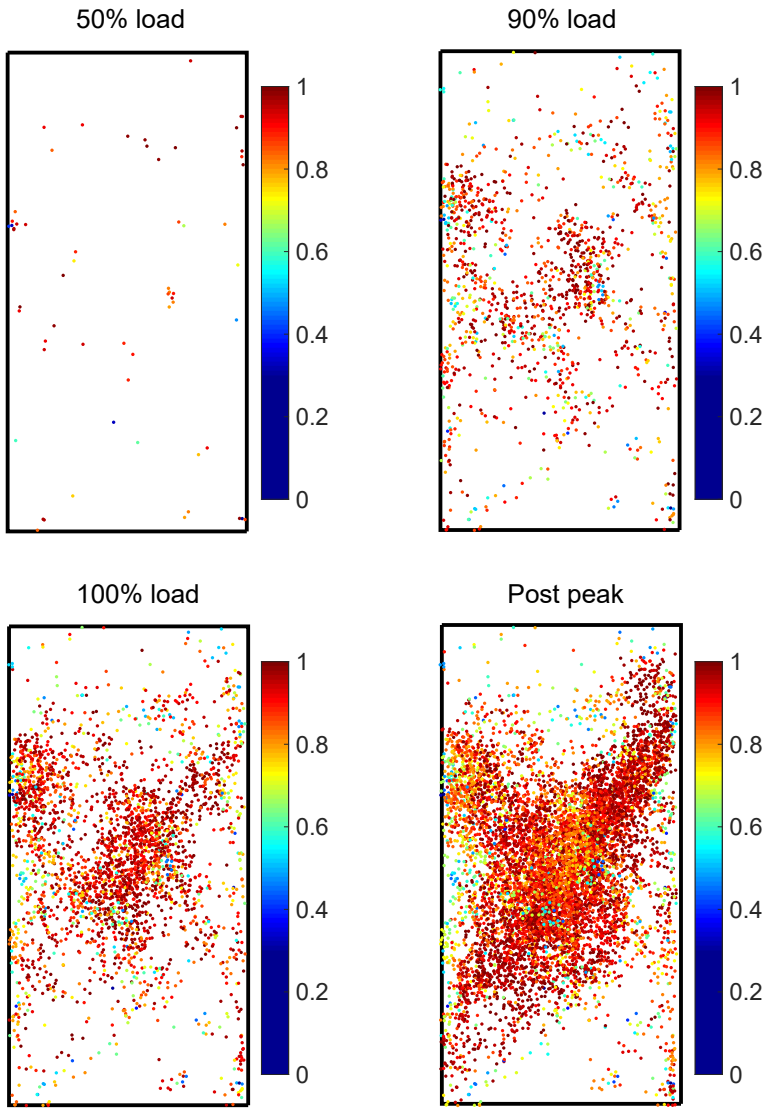

Figure 18: Micro-cracks in concrete at different stages of the uniaxial compression tests

5. Sensitivity of concrete strength to aggregates and ITZ properties

In Section 4, we calibrated our DEM model to reproduce the behavior of concrete, which, at same water/cement ratio, exhibited lower strength than mortar. The shape of coarse aggregates can affect concrete strength [68, 69]. In addition, it was noted that concrete strength decreases with the strength of coarse aggregates [3, 70], even though most studies focused on strong aggregates materials. What is more, some authors claim that the ITZ acts as a plane of weakness in concrete [1, 9]. The ITZ is a layer of around 15 to 30 μm that can only be observed through scanning electron microscopy (SEM); it is hence challenging to monitor the ITZ during concrete loading. Despite qualitative observations, quantitative analyses of the effects of aggregate characteristics on concrete strength are lacking. Therefore, in this section, we study the sensitivity of concrete strength to aggregate shape, aggregate strength and aggregate ITZ by simulating the BT and the UCT with our DEM model. We generate the DEM specimens following the method explained in Section 3.3 and we use the calibrated parameters listed in Table 4.

5.1. Effect of aggregate shape on concrete strength

Previous research shows that concrete containing angular crushed rock is stronger than concrete containing smooth gravel [71, 72]. In our model, aggregates are modeled with weaker bonds and softer particle elements, and shapes are determined by X-ray scanning. In order to evaluate the effect of aggregate shape on concrete strength, we simulate the response of a DEM

mortar sample with the same fractions of broken bonds (ITZ bonds), weaker bonds (aggregate inter-particle bonds) and softer particles (aggregate particles) as those of the calibrated DEM concrete samples, but with a random distribution of broken bonds, weak bonds and soft particles. The effect of aggregate shape on concrete strength is shown in Figures 19 and 20. When aggregate shape is ignored, the specimen can be regarded as a homogeneous material with uniformly distributed micro cracks and flaws. By contrast, in the concrete model that accounts for scanned aggregate shapes, the cracks and flaws are localized and higher stress concentrations occur. As a result, strength ranks as follows: mortar > concrete with uniformly distributed flaws (aggregate shape ignored) > concrete with scanned aggregate shapes. Simulation results show that the strength of concrete with scanned aggregate shapes is around 20% lower than of concrete with aggregate shapes ignored.

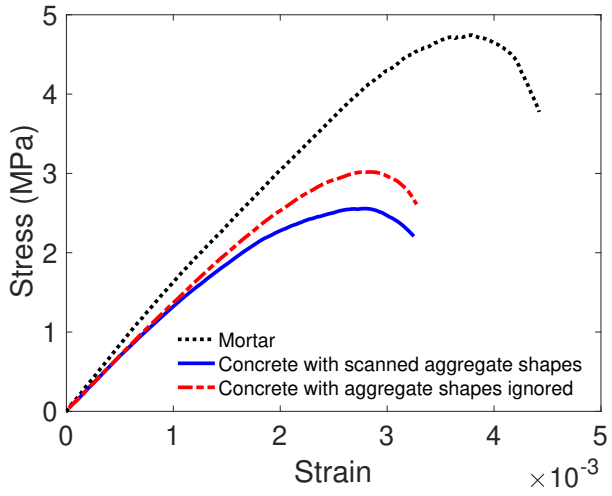

Figure 19: Effect of aggregate shape on concrete strength in Brazilian tests

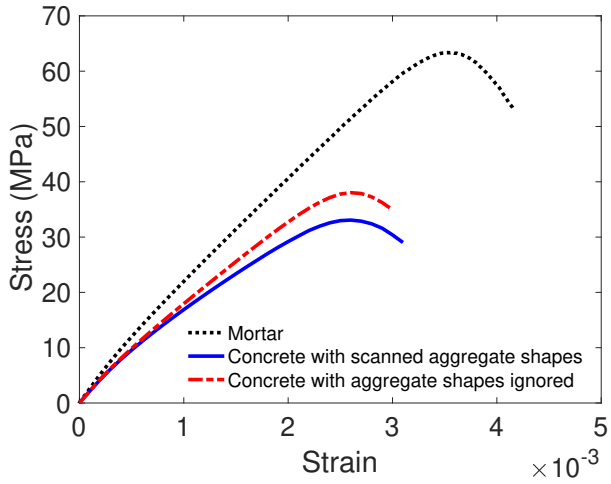

Figure 20: Effect of aggregate shape on concrete strength in uniaxial compression tests

5.2. Effect of aggregate tensile strength on concrete strength

According to the state-of-the-art, aggregates are expected to play an important role in concrete mechanical behavior. The calibrated tensile strength of the coarse aggregates is 3.5 MPa, which is lower than the mortar BTS. During the BTs and UCTs, we note indeed that concrete strength is lower than that of mortar, and we observe a large number of crushed aggregates. Materials commonly used for coarse aggregates include quartzite, limestone, marble, low strength granite and high strength granite. Corresponding aggregate tensile strengths span from 3.0 MPa up to 15.0 MPa [73, 74]. In order to understand the effect of aggregate tensile strength on concrete BTS and UCS, concrete specimens with different aggregate strengths are generated and subjected to BTs and UCTs. As mentioned in Section 4.2, we assume that the ultimate bond displacement at failure is the same for all aggregates, so that the change of aggregate strength dictates the change of

fracture energy, G_f. BT and UCT simulation results are shown in Figure 21 and 22, respectively. In general, concrete strength increases with aggregate strength, except in the simulation of the UCT with coarse aggregates with a tensile strength of 3.5 MPa. The exact reason for this unknown; this discrepancy may stem from the variability of concrete specimens generated with the DEM. Figures 23 and 24 show that the relationship between aggregate tensile strength and concrete strength is quasi-linear both in the BT and in the UCT. It it also noticeable that when the aggregate strength increases by more than 300%, concrete BTS and UCS increase by less than 68%.

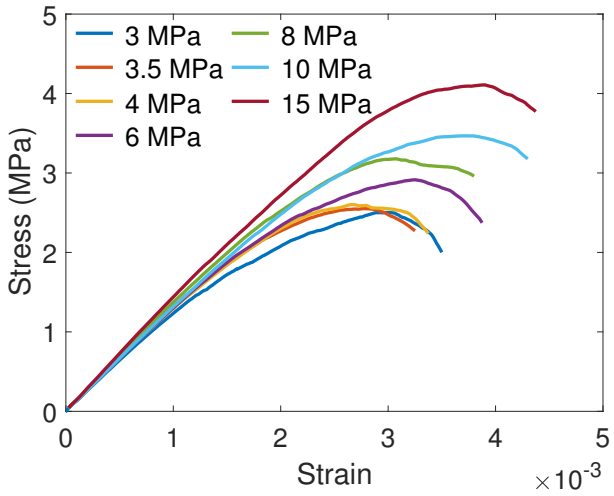

Figure 21: Stress-strain curves of concrete with different aggregate tensile strengths in the Brazilian tests

5.3. Effect of the Interfacial Transition Zone (ITZ) on concrete strength

In our model, the weakening effect of the ITZ is accounted for by deleting a fraction of the aggregate/mortar bonds. We define the contact ra-

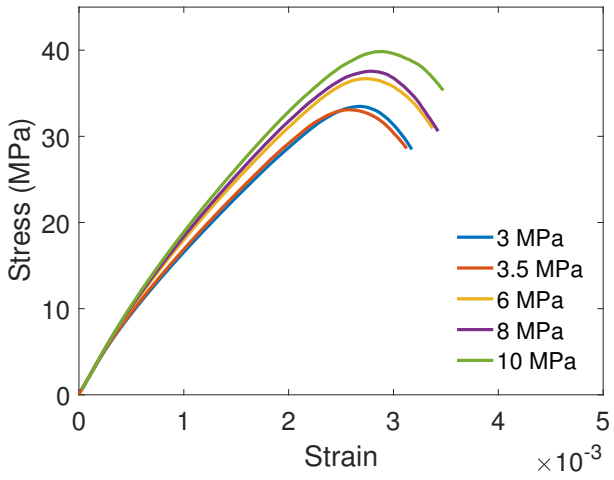

Figure 22: Stress-strain curves of concrete with different aggregate tensile strengths during the uniaxial compression tests

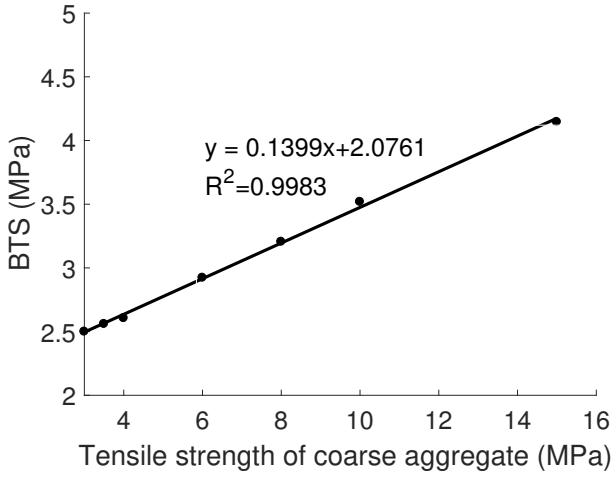

Figure 23: Effect of coarse aggregate tensile strength on concrete BTS

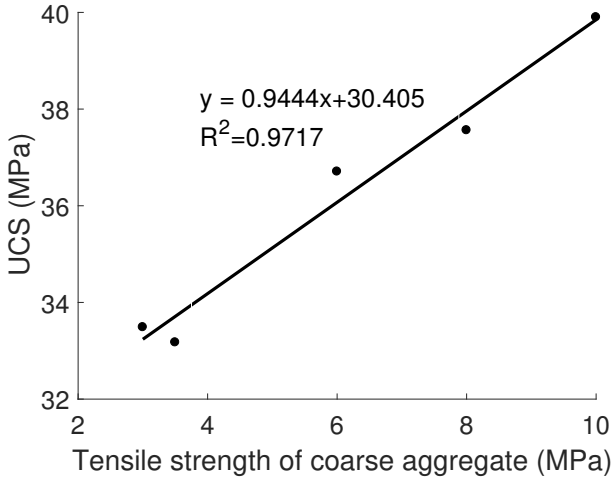

Figure 24: Effect of coarse aggregate tensile strength on concrete UCS

tio, α, as the number of displacement softening contact bonds used at aggregate/mortar interfaces over the total number of interfacial contacts.The model was calibrated for $\alpha = 80\%$. We now vary α between 50% and 100% to understand the influence of mortar/aggregate adhesive surface on concrete BTS and UCS. Results are presented in Figures 25 and 26, respectively. Note that for each contact ratio α we conducted the BT and UCT simulations at least three times. Only the average results are shown here. The ITZ greatly affects concrete strength: the BTS and the UCS respectively increase by 227.5% and 222.0% when α varies from 50% to 100%. The stress/strain curves are similar in all simulations: At first, stress increases with strain but the stiffness gradually decreases due to bond softening and breakage; Then stress reaches a peak value and the specimen starts to fail; As the specimen is further compressed, stress decreases rapidly and numerous bonds break. Figure 27 and 28 show that the strength-contact ratio relationship is lin-

ear for both the BT and the UCT. The higher α, the higher the strength. Contacts without displacement softening contact bonds can be viewed as internal micro-cracks or micro-flaws, similar to the ITZ in actual concrete. Micro-crack interaction and coalescence occur in specimens with low contact ratio, which drastically lowers concrete strength. To summarize, both the ITZ and aggregate tensile strength influence concrete strength, but concrete strength is most sensitive to the contact ratio α in the ITZ.

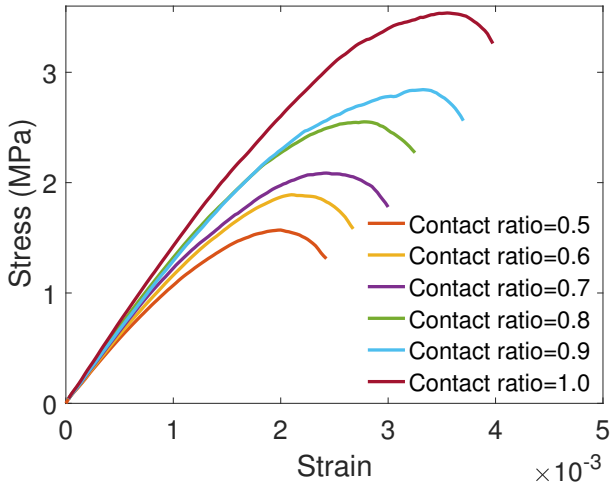

Figure 25: Stress-strain curves of concrete with different interface contact ratios in the Brazilian tests

6. Conclusions

We proposed a new bond displacement-softening law and implemented it in a DEM code to capture the behavior of mortar. We constructed DEM models of mortar and concrete by generating samples of bonded particles. First, the mechanical parameters of the spherical elements and of the dis-

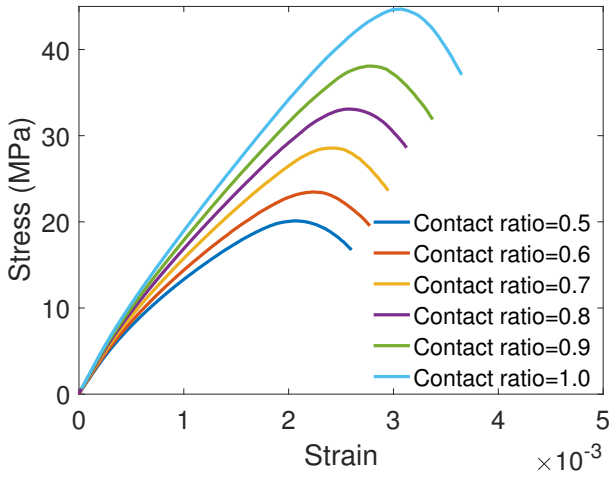

Figure 26: Stress-strain curves of concrete with different interface contact ratios in the uniaxial compression tests

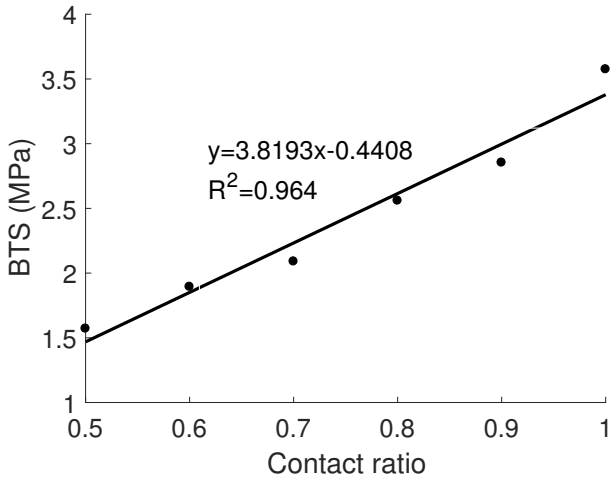

Figure 27: Effect of the interface contact ratio α on concrete BTS

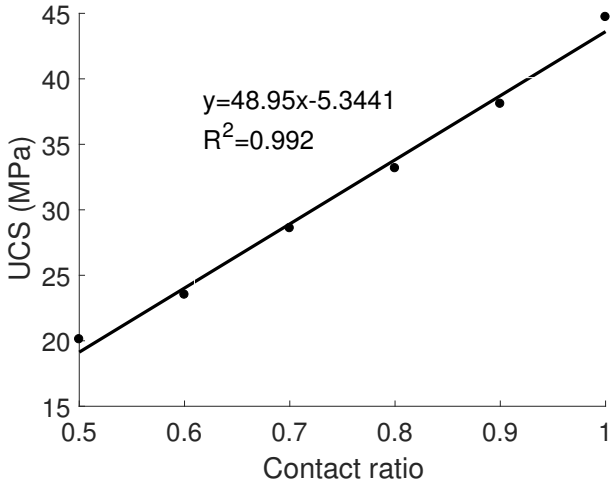

Figure 28: Effect of interface contact ratio α on concrete UCS

placement softening contact bond model were calibrated against mortar BT and UCT experiments. Then, coarse aggregates were generated from point clouds obtained by scanning actual aggregates used in concrete. The aggregate bond parameters were calibrated against concrete BTs and UCTs, with the calibrated mortar parameters. The proposed DEM models capture the mechanical behaviors of mortar and concrete, with a realistic ratio of UCS/BTS. We studied the influence of coarse aggregate characteristics. The main conclusions are the following:

1. Concrete BTS and UCS increase with aggregate tensile strength and with the ITZ contact ratio α.

   In our tests, mortar BTS and UCS are about twice as much as concrete BTS and UCS, respectively. Other authors had also noticed that concrete could have lower strength than mortar, and attributed this phenomenon to the weak surfaces in the ITZ. Our study confirms that

the ITZ is the primary cause of low concrete strength. Aggregate volume fraction is usually around 30% or more. We found that multiplying the aggregate tensile strength by four could increase concrete strength by 2/3. The effect of aggregate tensile strength on concrete strength had never been quantified before.

2. The proposed displacement softening contact bond model can capture mortar and concrete failure mechanisms in both the BT and the UCT. In the BT, micro-cracks first appear at the vicinity of the loading platens. But failure is induced by fractures that initiate at the center of the specimen and that coalesce with the cracks located close to the platens. Specimens subjected to UCTs exhibit multiple shear failure planes – usually, two symmetric shear bands. A realistic ratio of UCT/BT is obtained. Micro-parameters used in the proposed bond model are closely related to the macro-scale material properties, which facilitates calibration.
3. The ITZ is accounted for by deleting bonds at the mortar/aggregate interface. The ITZ can be seen as a distribution of interfacial micro-cracks, like in actual concrete. Both in the BT and the UCT, a linear relationship exists between the contact ratio α in the ITZ and concrete strength, for $0.5 \leq \alpha \leq 1.0$.
4. Aggregate shape plays an important role in the overall mechanical properties of concrete: for the same volume fraction of aggregate and the same specific surface of ITZ, concrete strength is 20% lower if aggregate shape is accounted for than if aggregate attributes are randomly distributed.

5. Concrete strength is linearly related to aggregate tensile strength. Weak aggregates decrease concrete strength. However, the influence of aggregate tensile strength on concrete strength is much lower than that of the ITZ.

The proposed softening displacement contact bond model is suitable to predict the behavior of concrete with the DEM. Results of the sensitivity analysis presented here suggest that increasing the adhesive area of the mortar/aggregate interface should improve the mechanical performance of concrete. Future studies will aim to understand the topological and physical factors that control the rheology of the aggregate/mortar interface.

Acknowledgements

Support for this research was provided by the Georgia Department of Transportation, as part of the project entitled "Mechanical integrity and sustainability of pre-stressed concrete bridge girders repaired by epoxy injection" (RP 16-24, RP 17-08 and RP 17-12).

References

[1] P. Monteiro, Concrete: microstructure, properties, and materials, McGraw-Hill Publishing, 2006.

[2] H. Beushausen, T. Dittmer, The influence of aggregate type on the strength and elastic modulus of high strength concrete, Construction and Building Materials 74 (2015) 132–139.

[3] J. Chi, R. Huang, C. Yang, J. Chang, Effect of aggregate properties on the strength and stiffness of lightweight concrete, Cement and Concrete Composites 25 (2) (2003) 197–205.

[4] F. Zhou, F. Lydon, B. Barr, Effect of coarse aggregate on elastic modulus and compressive strength of high performance concrete, Cement and Concrete Research 25 (1) (1995) 177–186.

[5] P.-C. Aïtcin, P. K. Mehta, Effect of coarse aggregate characteristics on mechanical properties of high-strength concrete, Materials Journal 87 (2) (1990) 103–107.

[6] S. Ahmad, S. A. Alghamdi, A study on effect of coarse aggregate type on concrete performance, Arabian Journal for Science and Engineering 37 (7) (2012) 1777–1786.

[7] H. Beshr, A. Almusallam, M. Maslehuddin, Effect of coarse aggregate quality on the mechanical properties of high strength concrete, Construction and building materials 17 (2) (2003) 97–103.

[8] A. Kılıç, C. Atiş, A. Teymen, O. Karahan, F. Özcan, C. Bilim, M. Özdemir, The influence of aggregate type on the strength and abrasion resistance of high strength concrete, Cement and Concrete Composites 30 (4) (2008) 290–296.

[9] K. L. Scrivener, A. K. Crumbie, P. Laugesen, The interfacial transition zone (itz) between cement paste and aggregate in concrete, Interface science 12 (4) (2004) 411–421.

[10] R. Zimbelmann, A contribution to the problem of cement-aggregate bond, Cement and Concrete Research 15 (5) (1985) 801–808.

[11] G. Prokopski, J. Halbiniak, Interfacial transition zone in cementitious materials, Cement and Concrete Research 30 (4) (2000) 579–583.

[12] C. Perry, J. Gillott, The influence of mortar-aggregate bond strength on the behaviour of concrete in uniaxial compression, Cement and Concrete Research 7 (5) (1977) 553–564.

[13] B. Chiaia, J. Van Mier, A. Vervuurt, Crack growth mechanisms in four different concretes: microscopic observations and fractal analysis, Cement and concrete research 28 (1) (1998) 103–114.

[14] J. Leite, V. Slowik, H. Mihashi, Computer simulation of fracture processes of concrete using mesolevel models of lattice structures, Cement and concrete research 34 (6) (2004) 1025–1033.

[15] J. Zhang, Z. Wang, H. Yang, Z. Wang, X. Shu, 3d meso-scale modeling of reinforcement concrete with high volume fraction of randomly distributed aggregates, Construction and Building Materials 164 (2018) 350–361.

[16] P. Wriggers, S. Moftah, Mesoscale models for concrete: Homogenisation and damage behaviour, Finite elements in analysis and design 42 (7) (2006) 623–636.

[17] X. Wang, M. Zhang, A. P. Jivkov, Computational technology for analysis of 3d meso-structure effects on damage and failure of concrete, International Journal of Solids and Structures 80 (2016) 310–333.

[18] J. F. Unger, S. Eckardt, C. Könke, Modelling of cohesive crack growth in concrete structures with the extended finite element method, Computer Methods in Applied Mechanics and Engineering 196 (41-44) (2007) 4087–4100.

[19] S. H. Song, G. H. Paulino, W. G. Buttlar, Simulation of crack propagation in asphalt concrete using an intrinsic cohesive zone model, Journal of Engineering Mechanics 132 (11) (2006) 1215–1223.

[20] M. G. Tijssens, B. L. Sluys, E. van der Giessen, Numerical simulation of quasi-brittle fracture using damaging cohesive surfaces, EUROPEAN JOURNAL OF MECHANICS SERIES A SOLIDS 19 (5) (2000) 761–780.

[21] M. Nitka, J. Tejchman, et al., Modelling of concrete fracture at aggregate level using fem and dem based on x-ray μct images of internal structure, Engineering fracture mechanics 147 (2015) 13–35.

[22] C. Qin, C. Zhang, Numerical study of dynamic behavior of concrete by mesoscale particle element modeling, in: Seismic Safety Evaluation of Concrete Dams, Elsevier, 2013, pp. 595–617.

[23] H. Kim, M. P. Wagoner, W. G. Buttlar, Simulation of fracture behavior in asphalt concrete using a heterogeneous cohesive zone discrete element model, Journal of Materials in Civil Engineering 20 (8) (2008) 552–563.

[24] W. Buttlar, Z. You, Discrete element modeling of asphalt concrete: microfabric approach, Transportation Research Record: Journal of the Transportation Research Board (1757) (2001) 111–118.

[25] X. Ding, L. Zhang, A new contact model to improve the simulated ratio of unconfined compressive strength to tensile strength in bonded particle models, International Journal of Rock Mechanics and Mining Sciences 69 (2014) 111–119.

[26] D. Potyondy, P. Cundall, A bonded-particle model for rock, International journal of rock mechanics and mining sciences 41 (8) (2004) 1329–1364.

[27] Y. Wang, F. Tonon, Modeling lac du bonnet granite using a discrete element model, International Journal of Rock Mechanics and Mining Sciences 46 (7) (2009) 1124–1135.

[28] M. P. Schöpfer, S. Abe, C. Childs, J. J. Walsh, The impact of porosity and crack density on the elasticity, strength and friction of cohesive granular materials: insights from DEM modelling, International Journal of Rock Mechanics and Mining Sciences 46 (2) (2009) 250–261.

[29] N. a. Cho, C. Martin, D. Sego, A clumped particle model for rock, International Journal of Rock Mechanics and Mining Sciences 44 (7) (2007) 997–1010.

[30] D. Potyondy, Parallel-bond refinements to match macroproperties of hard rock, in: Continuum and distinct element modeling in Geomechanics (Proceedings, 2nd Internationl FLAC/DEM Symposium): Itasca International, paper, 2011, pp. 08–04.

[31] Itasca, Particle Flow Code in Three Dimensions, Version 4.0., Itasca Consulting Group, Inc., Minnesota. (2008).

[32] Y. Sheng, D. Yang, Y. Tan, J. Ye, Microstructure effects on transverse cracking in composite laminae by dem, Composites Science and Technology 70 (14) (2010) 2093–2101.

[33] N. H. Nguyen, H. H. Bui, G. D. Nguyen, J. Kodikara, A cohesive damage-plasticity model for dem and its application for numerical investigation of soft rock fracture properties, International Journal of Plasticity 98 (2017) 175–196.

[34] Y. Ma, Discrete element modeling of the brittle-ductile transition in strength tests for quasi-brittle materials, Ph.D. thesis, Georgia Institute of Technology (2017).

[35] H. Kim, M. P. Wagoner, W. G. Buttlar, Numerical fracture analysis on the specimen size dependency of asphalt concrete using a cohesive softening model, Construction and Building Materials 23 (5) (2009) 2112–2120.

[36] Y. Ma, H. Huang, A displacement-softening contact model for discrete element modeling of quasi-brittle materials, International Journal of Rock Mechanics and Mining Sciences 104 (2018) 9–19.

[37] C. ASTM, et al., Standard test method for splitting tensile strength of cylindrical concrete.

[38] R. Berenbaum, I. Brodie, Measurement of the tensile strength of brittle materials, British Journal of Applied Physics 10 (1959) 281–287.

[39] Z. P. Ba¡ zant, M. Kazemi, Determination of fracture energy, process zone longth and brittleness number from size effect, with application

to rock and conerete, International Journal of fracture 44 (2) (1990) 111–131.

[40] Y. Ma, H. Huang, Dem analysis of failure mechanisms in the intact brazilian test, International Journal of Rock Mechanics and Mining Sciences 102 (2018) 109–119.

[41] D. Li, L. N. Y. Wong, The brazilian disc test for rock mechanics applications: review and new insights, Rock mechanics and rock engineering 46 (2) (2013) 269–287.

[42] A. Basu, D. Mishra, K. Roychowdhury, Rock failure modes under uniaxial compression, brazilian, and point load tests, Bulletin of Engineering Geology and the environment 72 (3-4) (2013) 457–475.

[43] A. ASTM, C39/c39m-18 standard test method for compressive strength of cylindrical concrete specimens. 2018, ASTM International: West Conshohocken, PA.

[44] F. Santarelli, E. Brown, Failure of three sedimentary rocks in triaxial and hollow cylinder compression tests, in: International Journal of Rock Mechanics and Mining Sciences & Geomechanics Abstracts, Vol. 26, Elsevier, 1989, pp. 401–413.

[45] A. Basu, T. B. Celestino, A. A. Bortolucci, Evaluation of rock mechanical behaviors under uniaxial compression with reference to assessed weathering grades, Rock Mechanics and Rock Engineering 42 (1) (2009) 73–93.

[46] Ł. Skarżyński, J. Tejchman, Experimental investigations of fracture process in concrete by means of x-ray micro-computed tomography, Strain 52 (1) (2016) 26–45.

[47] Z. P. Bazant, P. A. Pfeiffer, Determination of fracture energy from size effect and brittleness number, ACI Materials Journal 84 (6) (1987) 463–480.

[48] H. Nakamura, T. Higai, Compressive fracture energy and fracture zone length of concrete, Modeling of inelastic behavior of RC structures under seismic loads (2001) 471–487.

[49] P. Peterson, Fracture energy of concrete: Method of determination, Cement and Concrete research 10 (1) (1980) 79–89.

[50] C. Itasca, Pfc 3d-user manual, Itasca Consulting Group, Minneapolis.

[51] A. Fakhimi, T. Villegas, Application of dimensional analysis in calibration of a discrete element model for rock deformation and fracture, Rock Mechanics and Rock Engineering 40 (2) (2007) 193.

[52] E. Gallucci, K. Scrivener, A. Groso, M. Stampanoni, G. Margaritondo, 3d experimental investigation of the microstructure of cement pastes using synchrotron x-ray microtomography, Cement and Concrete Research 37 (3) (2007) 360–368.

[53] A. Committee, Building code requirements for structural concrete:(aci 318-99); and commentary (aci 318r-99), American Concrete Institute, 1999.

[54] Y. Xu, C. Xu, Z. Zhou, J. Du, D. Hu, 2D DEM simulation of particle mixing in rotating drum: A parametric study, Particuology 8 (2) (2010) 141–149.

[55] Z. P. Bazant, M. T. Kazemi, T. Hasegawa, J. Mazars, Size effect in brazilian split-cylinder tests: measurements and fracture analysis, ACI Materials Journal 88 (3) (1991) 325–332.

[56] C. Rocco, G. V. Guinea, J. Planas, M. Elices, Size effect and boundary conditions in the brazilian test: experimental verification, Materials and Structures 32 (3) (1999) 210.

[57] G. Giaccio, C. Rocco, R. Zerbino, The fracture energy (g f) of high-strength concretes, Materials and structures 26 (7) (1993) 381–386.

[58] E. N. Landis, E. N. Nagy, Three-dimensional work of fracture for mortar in compression, Engineering Fracture Mechanics 65 (2-3) (2000) 223–234.

[59] C. Rosselló, M. Elices, G. Guinea, Fracture of model concrete: 2. fracture energy and characteristic length, Cement and concrete research 36 (7) (2006) 1345–1353.

[60] F. Wittmann, Crack formation and fracture energy of normal and high strength concrete, Sadhana 27 (4) (2002) 413–423.

[61] H. Huang, B. Lecampion, E. Detournay, Discrete element modeling of tool-rock interaction i: rock cutting, International Journal for Numerical and Analytical Methods in Geomechanics 37 (13) (2013) 1913–1929.

arXiv:https://onlinelibrary.wiley.com/doi/pdf/10.1002/nag.2113, doi:10.1002/nag.2113.
URL https://onlinelibrary.wiley.com/doi/abs/10.1002/nag.2113

[62] M. S. Diederichs, The 2003 canadian geotechnical colloquium: Mechanistic interpretation and practical application of damage and spalling prediction criteria for deep tunnelling, Canadian Geotechnical Journal 44 (9) (2007) 1082–1116. arXiv:https://doi.org/10.1139/T07-033, doi:10.1139/T07-033.
URL https://doi.org/10.1139/T07-033

[63] A. Mardalizad, R. Scazzosi, A. Manes, M. Giglio, Testing and numerical simulation of a medium strength rock material under unconfined compression loading, Journal of Rock Mechanics and Geotechnical Engineering 10 (2) (2018) 197 – 211. doi:https://doi.org/10.1016/j.jrmge.2017.11.009.
URL http://www.sciencedirect.com/science/article/pii/S1674775517302524

[64] B. Park, K.-B. Min, N. Thompson, P. Horsrud, Three-dimensional bonded-particle discrete element modeling of mechanical behavior of transversely isotropic rock, International Journal of Rock Mechanics and Mining Sciences 110 (2018) 120 – 132. doi:https://doi.org/10.1016/j.ijrmms.2018.07.018.
URL http://www.sciencedirect.com/science/article/pii/S1365160917305567

[65] Z. P. Bazant, J. Planas, Fracture and size effect in concrete and other quasi-brittle materials, 1998.

[66] Y. D. Murray, A. Y. Abu-Odeh, R. P. Bligh, Evaluation of ls-dyna concrete material model 159, Tech. rep. (2007).

[67] W. Ren, Z. Yang, R. Sharma, C. Zhang, P. J. Withers, Two-dimensional x-ray ct image based meso-scale fracture modelling of concrete, Engineering Fracture Mechanics 133 (2015) 24–39.

[68] J.-S. Chen, M. Chang, K. Lin, Influence of coarse aggregate shape on the strength of asphalt concrete mixtures, Journal of the Eastern Asia Society for Transportation Studies 6 (2005) 1062–1075.

[69] C. Rocco, M. Elices, Effect of aggregate shape on the mechanical properties of a simple concrete, Engineering fracture mechanics 76 (2) (2009) 286–298.

[70] M. Kaplan, Flexural and compressive strength of concrete as affected by the properties of coarse aggregates, in: Journal Proceedings, Vol. 55, 1959, pp. 1193–1208.

[71] A. M. Neville, Properties of concrete, Vol. 4, longman London, 1995.

[72] Q. Li, Z. Deng, H. Fu, Effect of aggregate type on mechanical behavior of dam concrete, Materials Journal 101 (6) (2004) 483–492.

[73] A. Baykasoğlu, H. Güllü, H. Çanakçı, L. Özbakır, Prediction of compressive and tensile strength of limestone via genetic programming, Expert Systems with Applications 35 (1-2) (2008) 111–123.

[74] K.-R. Wu, B. Chen, W. Yao, D. Zhang, Effect of coarse aggregate type

on mechanical properties of high-performance concrete, Cement and Concrete Research 31 (10) (2001) 1421–1425.